Elucidating the Effect of Borate Additive in High-Voltage Electrolyte for Li-Rich Layered Oxide Materials

Yixuan Li, Weikang Li, Ryosuke Shimizu, Diyi Cheng, HongNam Nguyen, Jens Paulsen, Shinichi Kumakura, Minghao Zhang,* and Ying Shirley Meng*

Lithium-rich layered oxides (LRLO) have attracted great interest for high-energy Li-ion batteries due to their high theoretical capacity. However, capacity decay and voltage fade during the cycling impede the practical application of LRLO. Herein, the use of lithium bis-(oxalate)borate (LiBOB) as an electrolyte additive is reported to improve the cycling stability in high voltage LRLO/graphite full cells. The cell with LiBOB-containing electrolyte delivers 248 mAh g^{-1} initial capacity and shows no capacity decay after 70 cycles as well as 95.5% retention after 150 cycles over 4.5 V cycling. A systematic mechanism study for the LiBOB-enabled cycling performance improvement is conducted. Analytical electron microscopy under cryo-condition confirms the formation of a uniform interphase and less phase transformation on the LRLO particle, accompanied by less voltage decay in the cathode. The formation of B-F species is identified in the cycled electrolyte, elucidating the HF scavenger effect of LiBOB. Due to less HF corrosion on both electrode interphases, a reduced amount of transition metal dissolution and redeposition on the graphite is proved, thereby mitigating the capacity decay in LRLO/graphite full cells. These findings suggest that the borate additive is a promising strategy to optimize high voltage electrolyte for the industrialization of LRLO.

1. Introduction

Rechargeable lithium-ion batteries (LIBs) are considered to be one of the most important energy storage devices.[1] With the rapid growth of the electric vehicles market, the demand for high energy density LIBs is increasing.[2] Lithium-rich layered oxide (LRLO) as a high-energy cathode material has attracted many interests due to its large specific capacity (over 300 mAh g^{-1}).[3,4] Accompanied by Li extraction/insertion during charge and discharge, LRLO experiences not only the transition metal (TM) redox but also the oxygen redox which contributes a large portion to its high capacity.[5,6] Despite its high capacity, the practical deployment of LRLO is hindered by voltage fade and capacity decay during electrochemical cycling.[7,8] These two issues are correlated to the activation of oxygen redox at high voltage (>4.5 V versus Li$^+$/Li^0), which leads to surface and structure degradation during cycling, such as the formation of oxygen vacancies and irreversible oxygen loss,[8,9] the migration and the dissolution of TM,[10,11] the formation of spinel-like phase,[4] and the accumulation of microstrain.[12] Intensive materials modification efforts have been devoted to addressing the capacity and voltage decay issues in LRLO. Surface coating with oxides or fluorides such as Al$_2$O$_3$ and AlF$_3$ was applied to reduce the oxygen release and protect the surface from acidic species in the electrolyte.[13–15] Both cation and anion doping such as Mg, Mo, F were also designed to mitigate the capacity and voltage decay through the altering of electronic structure and the suppression of structural degradation.[16–18] Heat treatment and re-lithiation on cycled LRLO materials were also studied to recover the capacity and voltage decay after electrochemical cycling through the recovery of the honeycomb ordering in the TM layer.[19,20]

Besides the modification on active materials, many cell components have also been optimized for high-voltage operation such as the binder and conductive agents.[21] However, the compatibility of the electrolyte with the charged state of LRLO is often neglected in the literature. The activation step ubiquitously seen in anionic redox materials occurs at 4.5 V versus Li$^+$/Li^0. For the commonly used carbonate-based liquid electrolytes, when the voltage is pushed above this limit (4.5 V), the electrolytes decompose through the following processes: carbonate-based organic solvents such as ethylene carbonate (EC) oxidize and decompose at high voltage, accompanied by dehydrogenation reaction as the protons attached to the carbon in the carbonate solvents are dissociated.[22] The protons may further

Y. Li, W. Li, R. Shimizu, M. Zhang, Y. S. Meng
Department of NanoEngineering
University of California San Diego
La Jolla, CA 92093, USA
E-mail: miz016@eng.ucsd.edu; shirleymeng@ucsd.edu
D. Cheng, Y. S. Meng
Department of Materials Science and Engineering
University of California San Diego
La Jolla, CA 92093, USA
H. Nguyen, J. Paulsen
Umicore Korea
Chungeonam-do 31093, Republic of Korea
S. Kumakura
Umicore Japan
Minato, Tokyo 107-0061, Japan

ADVANCED
SCIENCE NEWS
www.advancedsciencenews.com

ADVANCED
ENERGY
MATERIALS
www.advenergymat.de

attack the cathode surface, binding with the oxygen on the cathode surface and generating H_2O.[23] Meanwhile, the autocatalytic decomposition of $LiPF_6$ leads to the formation of LiF and PF_5. The trace amount of H_2O from the fresh electrolyte and from carbonate solvent decomposition will then further react with PF_5 or $LiPF_6$ to produce acidic species such as HF.[24,25] In full cells with a high-voltage cathode and graphite anode, the produced HF will corrode the interphase between electrode and electrolyte, followed by the dissolution of TM from the cathode and its redeposition on the graphite.[26,27] These problematic behaviors from electrolyte decomposition significantly limit the lifetime of the high-voltage batteries. Many different strategies have been explored in the designing of high-voltage electrolytes as shown in **Figure 1**a. Inorganic and organic electrolyte additives were utilized in carbonate-based solvents since the decomposition of such additives may form stable CEI (cathode-electrolyte interphase) and SEI (anode-electrolyte interphase) to avoid further decomposition.[28–30] This strategy is cost-effective as the amount of additive is usually very low ($\approx$0.5–5%).[30,31] Good compatibility with graphite is also observed with this type of high-voltage electrolytes.[32,33] The utilization of high salt concentration electrolyte (HCE)[34] and the development of ionic liquids as electrolytes[35] have also been explored for high-voltage electrolytes, but both suffer from the high viscosity of electrolyte and in turn the bad wettability with thick electrodes. Fluorinated carbonates were also developed and used as the solvent for high-voltage electrolytes due to their high oxidation stability and thermal stability.[36–38] However, such fluorinated carbonate solvents are usually more expensive and may bring up the total cost of electrolytes compared to carbonate solvents.[39]

Replacement of carbonate-based solvents was also studied for high-voltage systems including the utilization of sulfone-based solvents[40,41] and nitrile-based solvents.[42,43] Those solvents are carbonate-free and generally have very high oxidation stability. However, the practical implementation of these electrolytes is challenging, due to the high viscosity in sulfone-based electrolytes and the low ionic conductivity in nitrile-based electrolytes, which make these electrolytes difficult to use for thick electrodes with high areal capacity loading.[33,40] As shown in Figure 1a, carbonate solvents with electrolyte additives show a balanced performance in different performance metrics required for high-voltage cells, while other strategies come with one or several weaknesses such as poor graphite compatibility, high viscosity, low ionic conductivity, low cost-effectiveness, etc.

In this work, lithium bis-(oxalate)borate (LiBOB) as an additive in the carbonate-based electrolyte was evaluated in LRLO/graphite full cells with thick electrodes (over 3 mAh cm^{-2} areal capacity loading). LiBOB was first synthesized by Xu et al.[44] and Lishka et al.[45] in two laboratories independently.[46] It shows many promising properties such as high thermal stability, ability to passivate aluminum substrates, and competence to form a stable SEI on graphite anode.[31,32,47,48] Recently, improved cycling stability was observed in many studies when LiBOB additive is utilized for high-voltage cathode materials such as $LiNi_{0.5}Mn_{1.5}O_4$ (LNMO),[49,50] $LiCoPO_4$,[51] and LRLO.[52,53] The performance improvement has been attributed to the formation of a passivation CEI containing borate species, which would inhibit the HF attack and electrolyte oxidation at high voltage.[36,54,55] In studies with LRLO/Li cells using LiBOB-containing electrolytes, other mechanisms have also been proposed such as the reduced
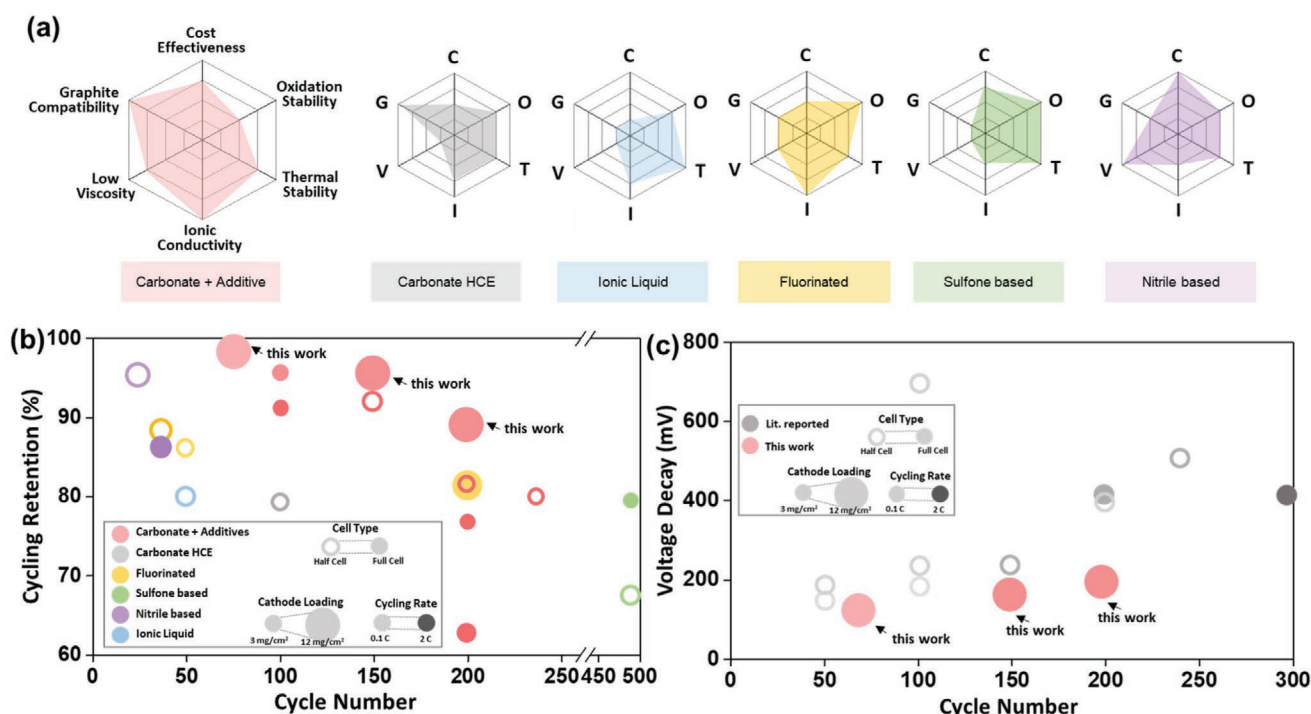

Figure 1. a) Performance metrics comparison of different types of novel high-voltage electrolytes; b) Literature summary of electrochemical performance of layered oxide materials cycled over 4.5 V in different novel electrolytes; c) Literature summary of the voltage decay for unmodified LRLO materials over long-term cycling.

amount of Li_2MnO_3 phase generation,[56] and the capturing of active oxygen species from the cathode surface.[52] However, the beneficial role of LiBOB for high-voltage battery systems has been mainly studied as its effect on the CEI so far. Not many works on full cells with graphite anode have been reported, not to mention a systematic evaluation of the full cell system including the cathode, the anode, and most importantly, the electrolyte. This is also because most of the literature reported work is conducted in coin cells, which makes it extremely hard to collect any cycled electrolyte for analysis.

In this work, we report the use of LiBOB in an LRLO/graphite full cell system with a 3 mAh cm^{-2} capacity loading, in both coin cell and pouch cell formats. A comparison of cell cycling performance with layered oxide materials cycled over 4.5 V between our results and literature reports is shown in Figure 1b with detailed information listed in Table S1, Supporting Information. Our designed full cell shows no capacity decay after 70 cycles at C/10. It also shows a capacity retention of 95.5% after 150 cycles and 89.5% after 200 cycles at C/5. Compared to most of the cells reported in literature with C/2 or even higher rate cycling, our cells with C/10 or C/5 were tested with prolonged time at high voltage, showing their superior cycling stability under extreme conditions. Moreover, the average discharge voltage decay of unmodified LRLO materials is compared between our results and literature reports, shown in Figure 1c with detailed information listed in Table S2, Supporting Information. Our cell shows a voltage decay of 196 mV for 200 cycles (1.0 mV per cycle), which is lower than other reported LRLO materials (usually over 1.4 mV per cycle for long-term cycling).[57–59] A detailed and systematic mechanism study was performed on different components from the cycled full cell including the cathode, the electrolyte, and the anode. We propose that the benefit of LiBOB additive in high voltage cycling comes from its scavenger effect with the HF generated in the electrolyte, thus leading to less HF corrosion on both CEI and SEI. The well preserved CEI also leads to less cathode surface/subsurface phase transformation and slows down the polarization increase in the cell, which all contribute to the alleviated voltage decay in LRLO cell.[60] With the good protection for both CEI and SEI, less graphite poisoning also take place during cycling, accompanied by the reduced amount of TM dissolution and TM deposition, resulting in the improved high voltage cycling stability in LiBOB-containing electrolyte.

2. Results and Discussion

2.1. Electrochemical Performance Comparison

SEM images of the pristine LRLO-UM are shown in Figure S1a,b, Supporting Information, where spheroid secondary particles with an average size of around 6 μm are observed. Synchrotron XRD pattern was collected for the pristine LRLO-UM for structural analysis. Rietveld refinement was performed on the collected XRD data to characterize the lattice parameters and site occupancies of the pristine LRLO-UM sample, shown in Figure S1c,d, Supporting Information. The sXRD pattern can be well indexed to the R-3m space group, with lattice parameter $a = 2.8418(3)$ Å and lattice parameter $c = 14.2470(3)$ Å. The refined

occupancies show a 1.59% Li/Ni mixing between the Li and TM layers. The superlattice peak at ≈6–7° in 2θ ($\lambda = 0.4579$ Å) corresponds to the short-range ordering of Li and TM atoms on a $\sqrt{3}a_{hex.} \times \sqrt{3}a_{hex.}$ honeycomb superlattice within the TM layer.[61,62] Overall, the LRLO-UM sample shows high material purity and a well-ordered layered structure with a small amount of Li/Ni mixing, which serves as a good baseline material in the study.

Electrochemistry tests were performed on LRLO-UM/graphite full cells with both baseline and LiBOB electrolyte. **Figure 2**a shows a similar charge and discharge voltage profile of the initial cycle of the full cells with different electrolytes. Both cells consist of a slope region around 4.1 V contributed by the TM redox, and a plateau region around 4.5 V ascribed to the oxygen redox.[63,64] At the first cycle, the baseline cell delivers 244 mAh g^{-1} discharge capacity and 858 Wh kg^{-1} energy density with 83.9% Coulombic efficiency (CE). The LiBOB cell delivers slightly higher capacity, energy density, and CE, which are 248 mAh g^{-1}, 874 Wh kg^{-1}, and 84.1%, respectively. Compared to other state-of-the-art cathode materials shown in Figure S2, Supporting Information,[65] LRLO materials can deliver a much higher specific capacity around 250 mAh g^{-1} as well as a much higher energy density around 850 Wh kg^{-1}. Unlike $LiCoO_2$ (LCO) which requires a large amount of Co, LRLO materials require a much lower price and offer the possibility of Co-free LRLO compositions. In addition, the high operating voltage in LRLO can effectively reduce the number of single cells used in each pack system, which will further improve the volumetric energy density.

The capacity and energy density of the LRLO-UM/graphite cells along with cycling are shown in Figure 2b,c. An obvious improvement of the cycling retention is observed with the LiBOB cell. The LiBOB cell shows no capacity decay within 70 cycles at a C/10 rate, compared to 76.3% capacity retention in the baseline cell. It is also observed that the CE and energy efficiency (EE) in the LiBOB cell is higher and more stable than the baseline cell. It is also noticeable that the LiBOB cell shows a Li_2MnO_3 activation period at 1–20 cycles while the baseline cell shows capacity decay from the beginning of cycling.[66] This indicates the continuous Li loss in the baseline cell upon cycling. With C/5 rate cycling, the LiBOB cell can achieve 95.5% retention of its initial discharge capacity after 150 cycles, as well as 89.5% capacity retention after 200 cycles, as shown in Figure S3, Supporting Information. Similar cycling retention improvements were also obtained with a series of LRLO materials with different compositions in both half cells and full cells, confirming that the LiBOB additive is generally applicable for high-voltage LRLO cells. The detailed material information and cycling performance of those cells are shown in Figure S4 and S5, Supporting Information. The average charge and discharge voltage and the dQ/dV curves of the LRLO-UM/graphite cells are shown in Figure 2d–f. The average discharge voltage of both baseline and LiBOB cells shows a slight decrease over cycling, which is well known as the voltage decay process for LRLO materials, coming from the structure degradation along with cycling.[10,67,68] Such a decay is also reflected as the overall peak shift to the low voltage range in the dQ/dV plots for both cells.[69] From the 2nd to the 70th cycle, the difference between the average charge and discharge voltage decreases 76 mV in the LiBOB cell, but it increases 65 mV in the baseline cell, representing a large increase in the voltage hysteresis and impedance
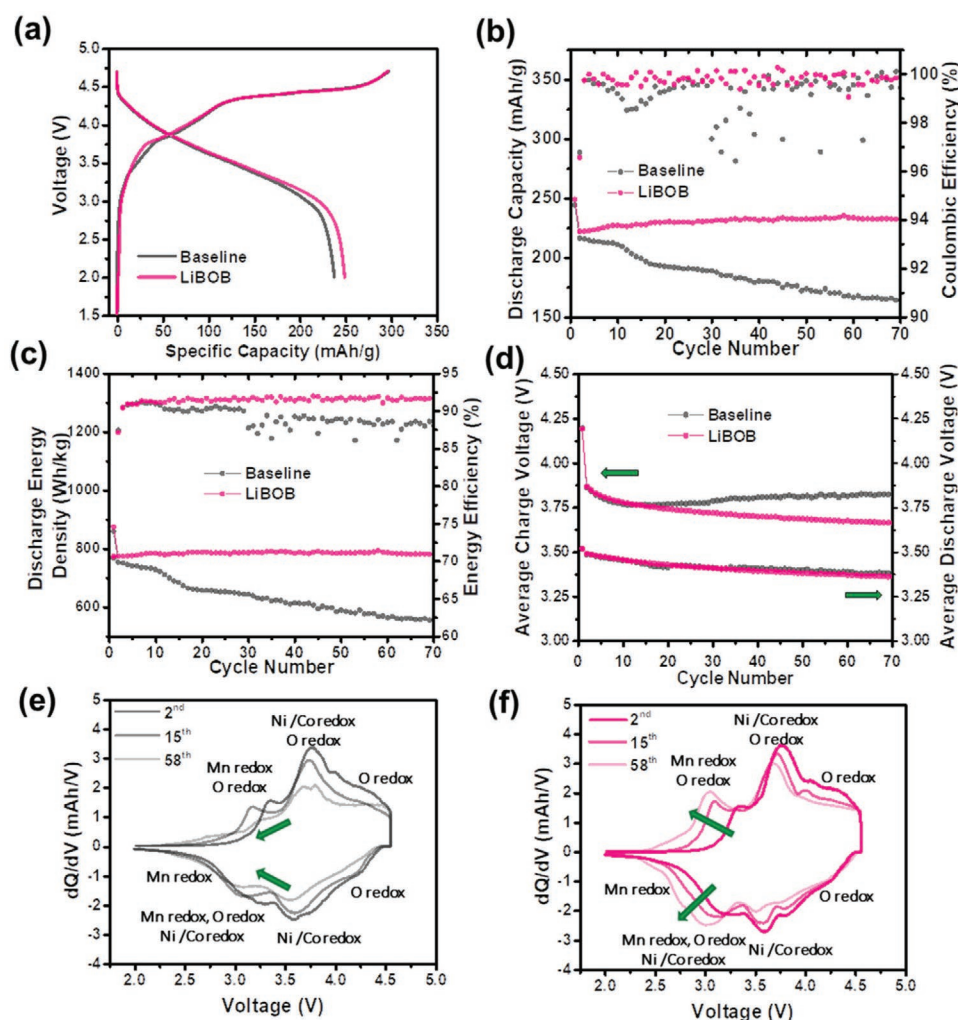
**ADVANCED
SCIENCE NEWS**
www.advancedsciencenews.com

**ADVANCED
ENERGY
MATERIALS**
www.advenergymat.de

Figure 2. Electrochemistry performance of LRLO-UM/graphite full cell with the baseline and LiBOB electrolyte: a) first cycle voltage profiles, b) discharge capacity and CE over cycling, c) discharge energy density and EE over cycling, d) average charge and discharge voltage over cycling, e) dQ/dV analysis of cell cycle in the baseline electrolyte, f) dQ/dV analysis of cell cycle in the LiBOB electrolyte. All cells are 3 mAh cm^{-2} level LRLO-UM/graphite full cells cycled with 2–4.7 V, C/20 for the first cycle, and 2–4.55 V, C/10 for the rest of cycling (1 C = 270 mA g^{-1}).

in the baseline cell.[70] In addition, the dQ/dV plot in the baseline cell shows an overall peak area shrinkage over cycling, indicating either the active material or Li inventory loss during cycling. During long-term cycling as shown in Figure S3, Supporting Information, the average discharge voltage decay for the LiBOB cell is only 1.2 mV per cycle, showing the ability of LiBOB electrolyte to alleviate LRLO cathode voltage decay. In summary, the addition of LiBOB in carbonate-based electrolytes evidently improves the cycling stability of LRLO/graphite full cells at high voltage.

2.2. Formation of Conformal CEI

Cryo-(S)TEM and EELS were performed on LRLO-UM cathode to evaluate the CEI formed in different electrolytes. Figure S6, Supporting Information shows the workflow of the cryo-STEM sample preparation, where a cross-section of the cathode sample is cut by a cryo-FIB, and a lamella of the cross-section is lifted out and thinned down for cryo-EM testing. This workflow can protect the CEI on the surface of spherical cathode particles to the largest extent. **Figure 3**a–c presents the cryo-STEM images of LRLO-UM at the pristine state, after cycling in the baseline electrolyte, and after cycling in the LiBOB electrolyte. At the pristine state, LRLO-UM shows a highly ordered structure with a clean surface. After 70 cycles in the baseline electrolyte, an inhomogeneous CEI layer with an average thickness of 1.5 nm can be observed on the LRLO-UM surface. Some parts of this particle surface have a CEI chunk with a thickness of 4.5 nm, while no CEI can be found on some other parts. As a comparison, a uniform CEI layer around 3.5 nm in thickness can be found on the LRLO-UM surface after 70 cycles in the LiBOB electrolyte. Cryo-TEM samples and cryo-FIB lamella samples were also prepared with the LRLO-NIMTE cathode from the half cells shown in Figure S4, Supporting Information. The corresponding cryo-EM images and analysis are shown in Figure S7, Supporting Information, where a more uniform and thicker CEI layer can also be observed with the LiBOB electrolyte. It
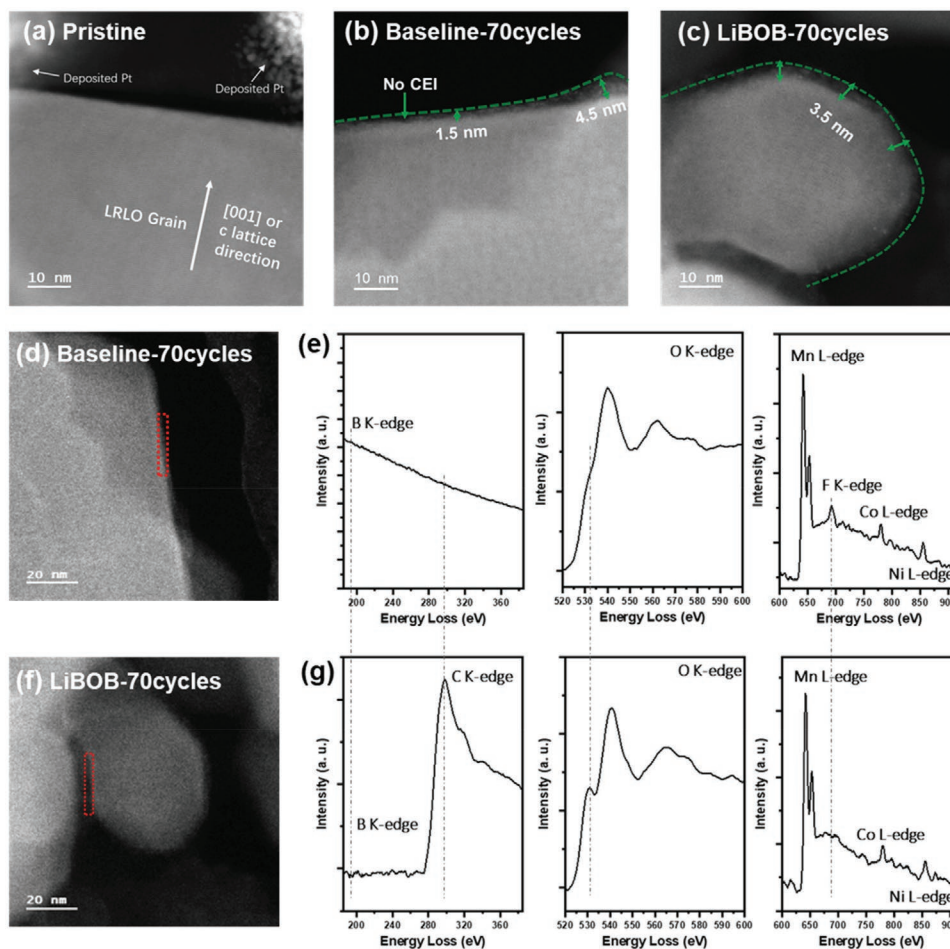
ADVANCED
SCIENCE NEWS
www.advancedsciencenews.com

ADVANCED
ENERGY
MATERIALS
www.advenergymat.de

Figure 3. Cryo-STEM images of the surface and/or CEI region of LRLO-UM cathode samples at different states: a) pristine, b) cycled in the baseline electrolyte, c) cycled in the LiBOB electrolyte. d–e) Cryo-EELS analysis of the CEI in the baseline electrolyte, the EELS spectra in (e) are collected from the red box region in (d). f–g) Cryo-EELS analysis of the CEI in the LiBOB electrolyte, the EELS spectra in (g) are collected from the red box region in (f).

is noticed that in the baseline electrolyte, the material loss and defect spinel phase formation is not limited to the surface, but evolving from the surface to subsurface and even bulk region with a maximum depth around 20 nm. In comparison, the well preserved cathode surface in the LiBOB cell suppresses the surface material loss and surface/subsurface phase transformation, thereby slowing down the polarization increase in the cell and mitigating the cathode voltage decay.[60] XPS analysis for the cathode surface is shown in Figure S9, Supporting Information. A much lower lattice oxygen peak is observed in the LiBOB cell compared to the baseline cell in Figure S9b, Supporting Information, indicating the formation of a more conformal CEI layer in the LiBOB cell.[49,71]

Observations of a thicker and more uniform CEI in the borate additive-containing electrolyte are in good agreement with various previous literature reports on both LNMO[49,72,73] and LRLO[52,74] cathode surface. For many of those studies focusing on the high-voltage system, the formation of a good CEI was attributed to the LiBOB salt decomposition upon cycling. Different mechanisms have been proposed in explaining the LiBOB decomposition pathways, such as through the loss of one electron per LiBOB and followed by radical coupling

reaction;[72] or through the loss of two electrons per LiBOB and followed by the binding with oxygen radicals.[52] After all, the decomposition of LiBOB would lead to the formation of a CEI layer containing boron species, which serves as a passivation film and slows down the side reactions at high voltage on the cathode and improves the cycling stability. In this work, to obtain the chemical information of the CEI on the cathode surface formed in different electrolytes, cryo-STEM-EELS are collected and shown in Figure 3d–g. Surprisingly, no boron signal is found from the CEI in the LiBOB electrolyte at B K-edge. At C K-edge, a large amount of carbon signal can be observed in the LiBOB cell but not in the baseline cell, implying that at least at this tested location, the carbonate-based CEI is maintained very well in the LiBOB electrolyte. At O K-edge, a clear pre-edge peak can be observed in the LiBOB cell but not in the baseline cell. This pre-edge peak originates from the Mn 3d-O 2p electron orbital hybridization, and the disappearance of this peak in the baseline cell suggests the reduced covalency between Mn and O, corresponding to the surface/subsurface phase transformation.[56,75] At F K-edge, a clear fluorine signal is observed from the CEI in the baseline electrolyte but not in the LiBOB electrolyte. This fluorine signal in the baseline cell can be a

result of HF attacking the cathode surface and the LiF generation,[76,77] which is in line with the low carbon signal observed at C K-edge as a result of HF corrosion on the CEI. These findings also agree with the increased cell impedance in the baseline cell as suggested in Figure 1d, coming from the etched material surface, the surface/subsurface phase transformation, and the accumulation of LiF. To summarize the characterization results for CEI, a thicker and more uniform CEI are formed on the cathode surface in the LiBOB electrolyte, accompanied by less phase transformation of the LRLO-UM material. Here we also want to point out that although (S)TEM is a characterization tool to probe local structure and chemical information, our observations are conducted with statistics since multiple particles in Figure S7 and S8, Supporting Information are showing similar results of the conformal CEI formed on the cathode surface after cycling in LiBOB electrolyte. Surprisingly, this CEI layer in the LiBOB electrolyte does not contain boron-based species. In previous literature reports, the chemical information of the as-hypothesized boron-containing passivation CEI was mainly evaluated through the following evidence: increased semi-carbonate species observed in XPS C 1s spectra,[73] boron signal presented in XPS B 1s spectra,[56] and reduced electrolyte decomposition products confirmed through FTIR.[72,73] However, the carbon signal in XPS C 1s and FTIR results are not direct evidence of boron in CEI, hence they may just represent the suppression of electrolyte decomposition and good preservation of CEI in the LiBOB electrolyte. In addition, the B 1s region is intrinsically overlapping with the P 2s region in XPS, making it difficult to ascribe the observed signal to boron species or phosphide that are largely contained in $LiPF_6$ based electrolytes. To the best of our knowledge, this work for the first time employs cryo-STEM-EELS in the analysis of the chemical environment in CEI and confirms that no boron signal is presented in CEI. To locate the boron species after cycling, further characterization is required on other components of the full cell system such as the electrolyte and graphite anode.

2.3. B-F Chemistry in LiBOB Electrolyte

To further investigate the underlying mechanism for the cycling stability improvement and the existence of boron species in the LiBOB cell, the cycled electrolyte needs to be carefully studied. Since it is tough to extract any remaining electrolyte after cycling from coin cells, we fabricated a single-layer LRLO-UM/graphite pouch cell for the electrolyte characterization. The design and testing setup for the pouch cells are shown in Figure S10, Supporting Information and the electrochemistry performance of the pouch cells is shown in Figure S11, Supporting Information. A stacking pressure of 416 kPa on the electrode area was accurately applied to the pouch cell during the cycling to ensure good electrochemical contact. In the first cycle, the LRNCM/graphite pouch cells deliver a similar discharge capacity compared to the coin cells. For the following cycles, the pouch cells also show good consistency with the coin cells, where a continuous decay for the baseline cell but a stable cycling for the LiBOB cell is observed. The hysteresis growth in the baseline electrolyte can also be observed in pouch cells. After 50 cycles, the pouch cells were disassembled and the

cycled electrolytes were extracted inside the Ar-filled glovebox for characterizations.

ICP-MS was performed on the fresh and cycled electrolytes for elemental concentration analysis, and the results are shown in **Figure 4**a. For both the baseline and LiBOB electrolyte, a lithium concentration around 7–8 g l^{-1} is detected at fresh state, in line with the designed 1 M Li salt concentration in the electrolyte. A slight decrease of Li concentration is observed after cycling in both electrolytes, which may be attributed to the loss of Li through CEI/SEI formation.[78] The boron concentration is similar in the LiBOB electrolyte before and after cycling. This indicates that the majority of the boron stays in the electrolyte during cycling, which explains why no boron signal was observed in the cryo-STEM-EELS analysis of the CEI. Further investigation on possible boron species in the electrolyte will be conducted in the latter part of this work. It is also noticed that in the fresh baseline and LiBOB electrolyte, no TM signals can be detected through ICP-MS. After cycling, less TM dissolution, especially less Mn dissolution, is observed in the LiBOB electrolyte. A similar decrease in TM deposition on the anode has also been reported in LNMO/graphite system with LiBOB-containing electrolyte before.[79] KF Titration was performed with both electrolytes at the fresh state and after cycling, where a similar moisture level is detected across all the samples. However, this does not mean that the same amount of moisture is generated during cycling for both electrolytes because the moisture can react with $LiPF_6$ right after formation.

To further quantify the salt composition in the electrolyte, ^{19}F NMR was conducted on the fresh and cycled electrolytes. Figure 4b shows the full range of the ^{19}F NMR spectra, where a strong doublet is observed at –72.4 ppm, corresponding to the $LiPF_6$ salt from the electrolyte.[80] For baseline electrolyte, the amount of $LiPF_6$ is smaller in the cycled sample compared to the fresh sample, as suggested by the area integration of $LiPF_6$ species shown in Table S6, Supporting Information. This indicates the $LiPF_6$ decomposition after cycling. Figure 4c shows the magnified region around –150 ppm for B-F species.[81] The baseline electrolytes show no signal in this region. The just-prepared LiBOB electrolyte also barely shows any signals. However, clear peaks are seen in the fresh LiBOB electrolyte after storage and grow even higher after cycling. These signals at –150.9 ppm and –153.2 ppm are assigned to lithium tetrafluoroborate ($LiBF_4$) and lithium difluoroborate (LiDFOB), respectively.[82,83] Since only 2 wt% of LiBOB was added to the baseline electrolyte, these B-F peaks are very small compared to the $LiPF_6$ signal. The generation of $LiBF_4$ and LiDFOB in fresh LiBOB electrolyte after storage can be attributed to the effect of the thermal reaction of $LiPF_6$ in presence with LiBOB, where disproportionation reaction happens between the fluoride ligands on phosphorus (in $LiPF_6$) and the oxalato ligands on boron (in LiBOB).[84] Compared to the fresh LiBOB electrolyte after storage, the amount of B-F species largely increases in the cycled electrolyte, indicating that other reactions occur between LiBOB salt and fluoride in the electrolyte under high voltage cycling. During cycling, it is commonly acknowledged that $LiPF_6$ decomposition and PF_5 hydrolysis can lead to the generation of large amount of acidic species such as HF, which corrodes the CEI and SEI in the cell and degrades the battery performance.[25,85] When LiBOB additive is used in the electrolyte,
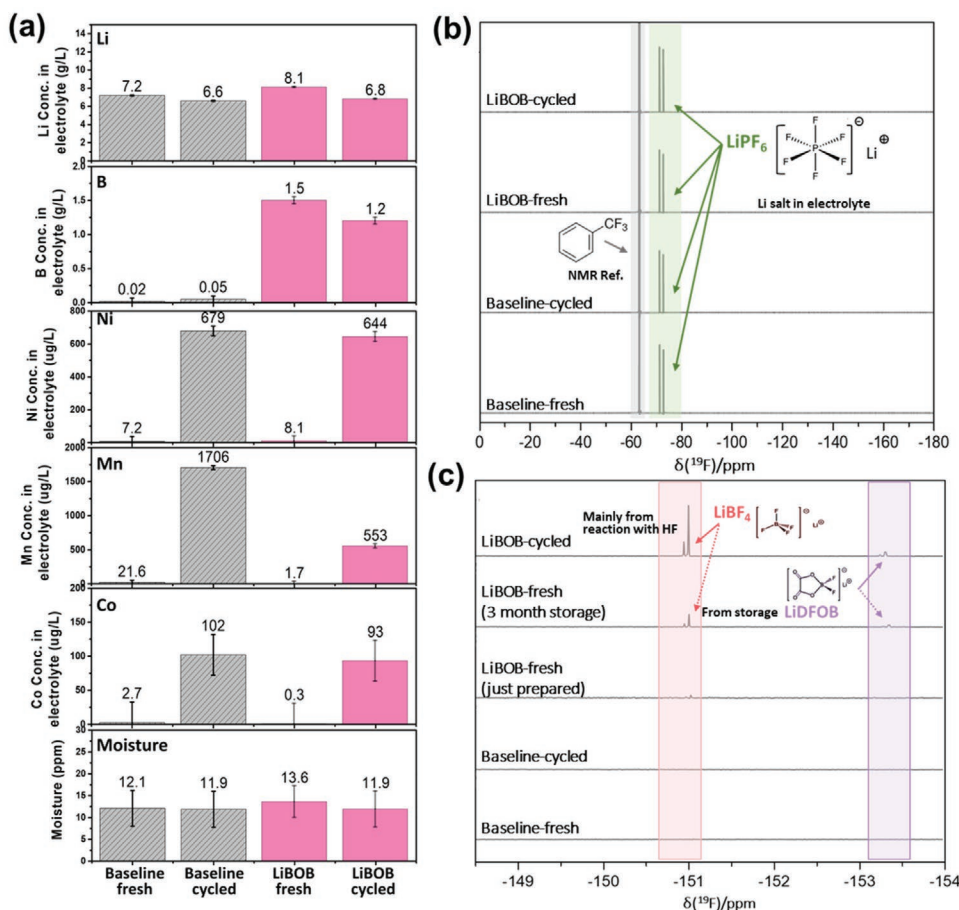
**ADVANCED
SCIENCE NEWS**

www.advancedsciencenews.com

**ADVANCED
ENERGY
MATERIALS**

www.advenergymat.de

Figure 4. Characterizations of the baseline and LiBOB electrolyte at the fresh state and after 50 cycles in pouch cells. a) Element concentration of Li, B, Ni, Co, Mn obtained from ICP-MS and moisture level obtained from Karl-Fischer test, b) ^{19}F NMR spectra at full scan, c) ^{19}F NMR spectra at the magnified region for B–F bonding.

it decomposes upon charging. The LiBOB salt or borate radicals from LiBOB decomposition can then directly react with HF, which is the source of $LiBF_4$ observed in NMR. Similar B-F species generation was also reported in $LiNi_{0.5}Mn_{0.3}Co_{0.2}O_2$ (NMC532) anode-free pouch cells using other borate additives in the electrolyte.[82,86] In summary of the CEI and electrolyte characterizations, the majority of B stays in the electrolyte during cycling rather than forming a B-enriched CEI on the cathode surface. Upon cycling, LiBOB in the electrolyte serves as the HF scavenger that inhibits the generation of HF and its corrosion on the interphase, leading to less TM dissolution from the cathode surface. In other words, the observed uniform and stable CEI in the LiBOB-containing electrolyte is the result of reduced HF corrosion.

2.4. Mitigated TM Dissolution and Redeposition

A reduced amount of HF in the electrolyte would also lead to less corrosion of the SEI and less TM deposition on the graphite anode, which will be further characterized in this section. The surface morphology of graphite after cycling in the baseline and the LiBOB electrolyte is similar to the pristine state, as suggested

by the SEM images in Figure S12, Supporting Information. EDX was performed on the graphite electrodes to measure the elemental distribution on the graphite surface, shown in **Figure 5**a,b. At the pristine state, only carbon and copper (current collector for graphite electrode) signals are detected. After cycling, EDX suggests the appearance of oxygen, fluorine, phosphorus, manganese, cobalt, and nickel on the graphite surface in both electrolytes. The TM (Mn, Co, and Ni) signals are much less on the graphite cycled in the LiBOB cell than in the baseline cell, indicating less TM deposition on the graphite in the LiBOB electrolyte. This is in good agreement with the ICP-MS analysis of the electrolyte, where less TM dissolution was also observed in the cycled LiBOB electrolyte. The overall mass loss from the cathode side is less in the LiBOB electrolyte compared to the baseline electrolyte, also contributing to the improved cycling stability of the LiBOB cell. Moreover, the fluorine amount on the graphite surface in the baseline electrolyte is higher than that in the LiBOB electrolyte, which is in line with the STEM-EELS results on the CEI side. The high fluorine signal on both CEI and SEI analysis suggests more $LiPF_6$ decomposition and HF corrosion in the baseline electrolyte.

XPS is employed to further explore the surface chemistry of graphite at the pristine state, soaked and cycled in
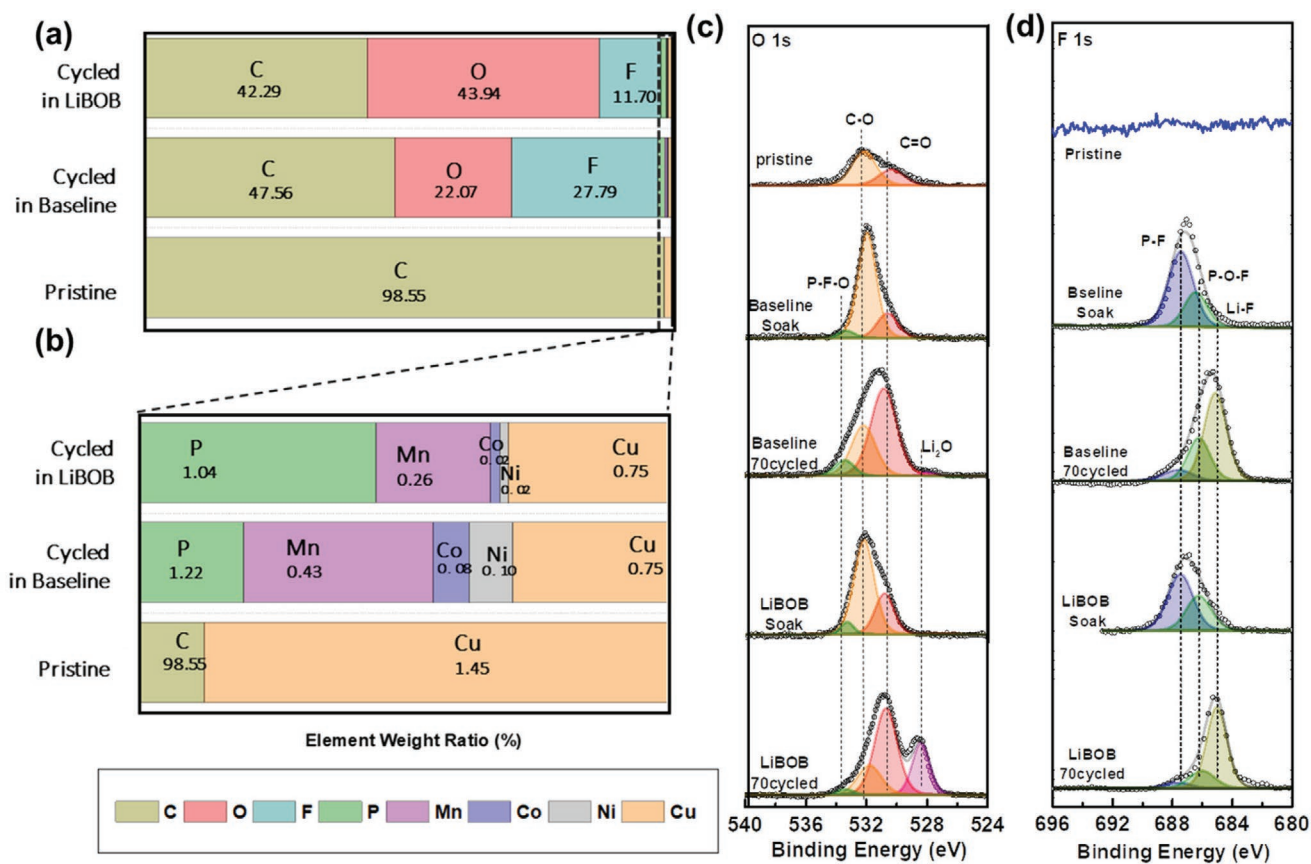
Figure 5. Characterization of SEI species on graphite at the pristine state, cycled in the baseline electrolyte, and cycled in the LiBOB electrolyte from the LRLO-UM/graphite full cells. a) Element weight ratio obtained from SEM-EDX; b) Magnified region from Figure 5(a) for TM deposited on the graphite surface; c) XPS comparison at O 1s spectra; d) XPS comparison at F 1s spectra.

both electrolytes. Figure 5c,d shows the O 1s spectra and the F 1s spectra. For O 1s spectra, the peaks at 533.8 eV, 532 eV, 530.7 eV, and 528.3 eV are assigned to P–F–O ($Li_xPF_yO_z$ from $LiPF_6$ decomposition), C–O, C=O, and Li_2O species, respectively.[87,88] A large amount of Li_2O can be found in the cycled LiBOB cell but not in the baseline cell. Since Li_2O is a common component for SEI and is highly sensitive to the presence of HF and H_2O,[89] the higher amount of Li_2O in the LiBOB electrolyte indicates a better SEI formation and lower moisture/HF level in the LiBOB cell. For F 1s spectra, the peaks at 687.8 eV, 686.1 eV, and 685 eV are assigned to P–F (from $LiPF_6$), P–O–F ($Li_xPF_yO_z$ from $LiPF_6$ decomposition), and LiF species, respectively. No F species are detected on the pristine graphite surface. After cycling, the generation of LiF and $Li_xPF_yO_z$ are observed on graphite surface cycled in both electrolytes, but the amount of $Li_xPF_yO_z$ is much less in the LiBOB case, indicating less $LiPF_6$ decomposition. Figure S13, Supporting Information shows the rest of the XPS fitting results for the same set of graphite electrodes. For C 1s spectra, the increased C=O peak at 288.9 eV in the LiBOB cell may indicate the decomposition of LiBOB and the generation of semi-carbonate species.[90–92] In addition, clear Mn 2p and Ni 2p signals were detected on graphite cycled in the baseline electrolyte but not in the LiBOB electrolyte, showing that LiBOB electrolyte can effectively suppress TM dissolution and deposition in high-voltage systems.

This result also agrees with the increased TM signals on the graphite surface from the baseline electrolyte shown in EDX.

2.5. Elucidating the HF Scavenger Effect of LiBOB

To summarize the characterization results on the different components of the LRLO-UM/graphite full cell system, a mechanism for explaining the improved high-voltage cell performance in LiBOB electrolyte is proposed and illustrated in **Figure 6**. The decomposition of carbonate-based electrolyte at high voltage is shown in Figure 6a with EC molecules as an example. During the high voltage charge process, electrons are extracted from the cathode as Li ions move out of active materials. However, such high voltage may also pull electrons from EC and cause the oxidation and structure breaking of EC molecules.[93] With the ring opening of EC, the formation of CO_2 gas and the generation of free protons also take place with the participation of a trace amount of H_2O in the fresh electrolyte.[94–96] The generated free protons may further attack the cathode surface, binding with the oxygen on the cathode surface and generating more H_2O.[23] The H_2O will then hydrolyze the $LiPF_6$ salt or PF_5 in the electrolyte and form HF, which would, in turn, corrode the CEI and the oxide cathode to generate even more H_2O.[25] These reactions form a vicious circle
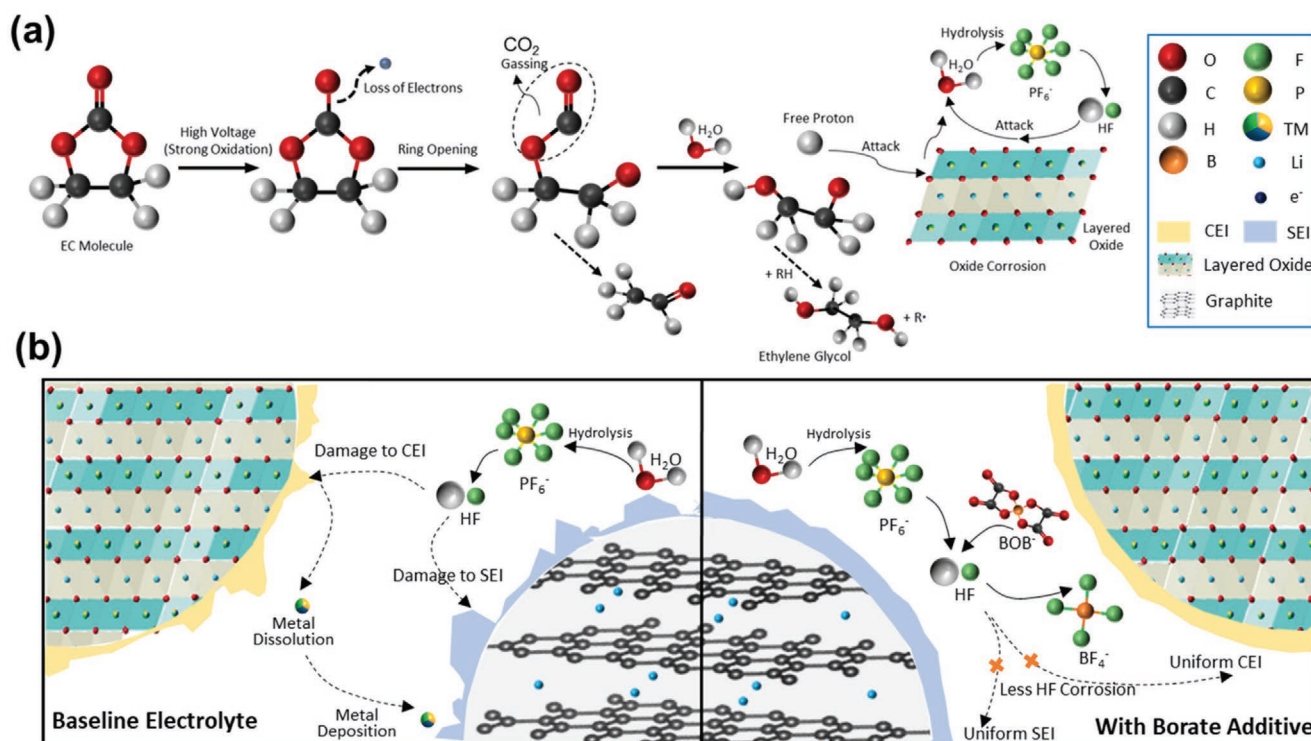
Figure 6. Schematic of a) carbonate-based electrolyte decomposition in high-voltage layered oxide system using EC as an example; b) enhanced cell performance for borate additive electrolyte in high-voltage full cell system.

and contribute to a large portion of cell performance degradation. Since HF can continuously corrode both the CEI and SEI during cell cycling, the cell will suffer from lithium inventory loss to compensate for the continuous new CEI/SEI formation. Furthermore, as the cathode oxides get corroded, some TM cations dissolute to the electrolyte and deposit on the graphite, which contributes to graphite poisoning.[26] This is also referred to as the cross-talk between cathode and anode in full cells.[27] The left part in Figure 6b summarizes these cell degradation factors in the baseline electrolyte including HF generation and corrosion on cell components, CEI/SEI damage and regrowth, TM dissolution and redeposition, graphite poisoning, etc. The generation of HF plays a crucial role in performance degradation and leads to poor cycling performance for high-voltage cells. In this work, we seek to clarify the mechanism for the improved cycling stability for high-voltage cells with the borate additive-containing electrolytes. Our results are highly consistent with many previous literature reports on high-voltage cathode materials that a more uniform and thicker CEI can be detected on the cathode surface in the borate-containing electrolytes. However, the uniform CEI may be the result of less HF attack, instead of the reason for preventing HF corrosion as suggested in many papers. Through a series of characterization tools on the cathode, the electrolyte, and the anode component in the full cell system, HF corrosion is found to be the main cause of CEI and SEI damage in carbonate-based electrolytes, and borate additives can effectively improve the cell cycling performance by suppressing the HF corrosion. This mechanism is depicted in the right part of Figure 6b. When LiBOB presents as an additive in carbonate-based electrolytes, the LiBOB salt or

borate radicals from LiBOB decomposition can effectively serve as the HF scavenger through the formation of B–F species. Note that the formation energy of BF_4^- (-1710 kJ mol^{-1})[90] is much lower than HF (-273 kJ mol^{-1}),[97] so this reaction would be thermodynamically favorable. In addition, B-F (613 kJ mol^{-1}) has much higher bond energy than H–F (565 kJ mol^{-1}) and P-F (490 kJ mol^{-1}), meaning that the B–F bond is more stable than H–F and P–F bond.[98] This is also in line with the increased stability of $LiBF_4$ than $LiPF_6$ reported in the literature.[99] As a result, less HF corrosion happens in the LiBOB electrolyte, leading to the presence of uniform CEI/SEI layers in the cell. The well preserved CEI/SEI then results in a reduced amount of cathode surface/subsurface phase transformation and less voltage decay as well as less TM dissolution and deposition in the cell, which all contributes to the improved cell cycling stability in the LiBOB electrolyte.

3. Conclusion

LiBOB is studied as an electrolyte additive in a high-voltage full cell system with an LRLO cathode and graphite anode with a 3 mAh cm^{-2} areal capacity loading. With 2 wt% of LiBOB added to the carbonate-based electrolyte, the LRLO-UM/graphite full cell shows 25% more capacity retention in the LiBOB-containing electrolyte than in the baseline electrolyte after 70 cycles. After 150 cycles with C/5, the cell only exhibits 185 mV voltage decay and can still deliver 95.5% of its original capacity. The mechanism for the cycling stability improvement with the LiBOB electrolyte is studied with a systematic analysis

ADVANCED
SCIENCE NEWS
www.advancedsciencenews.com

ADVANCED
ENERGY
MATERIALS
www.advenergymat.de

of the cathode, the electrolyte, and the anode from the cycled full cells. Cryo-EM and XPS confirm less surface/subsurface phase transformation and a more uniform and thicker CEI on the cathode surface in the LiBOB electrolyte, which may be beneficial in stabilizing the polarization increase in the cell and mitigating the voltage decay in the cathode. However, this CEI is not boron-based and the majority of boron stays in the electrolyte after cycling. NMR confirms the generation of LiDFOB and LiBF$_4$ in the electrolyte during cycling, which comes from the reaction between LiBOB or borate radicals and HF generated from electrolyte decomposition. The reduced amount of HF corrosion in the LiBOB electrolyte also leads to a more uniform SEI on the graphite surface. With less HF attack on both CEI and SEI, less TM dissolution into the electrolyte and less TM deposition on the graphite is observed in the full cell with LiBOB electrolyte. Overall, LiBOB serves as the HF scavenger in high-voltage cells, which leads to less HF corrosion on both electrodes and therefore improved cycling stability in LRLO/ graphite full cells. These findings may also be applied to other high-voltage systems besides layered oxides, such as spinel LNMO or LiCoMnO$_4$, olivine LiCoPO$_4$, etc., thus opening a door for the commercialization of those high-voltage materials. This work also inspires the future exploration of other scavenging materials that can stabilize the LiPF$_6$-containing carbonate-based electrolytes through the elimination or deactivation of the reactive substances generated in electrolyte decomposition processes.

4. Experimental Section

Electrochemistry Tests: Pristine Li$_{1.18}$Ni$_{0.18}$Co$_{0.09}$Mn$_{0.55}$O$_2$ sample (denoted as LRLO-UM) was provided by Umicore. The pristine material was mixed with polyvinylidene fluoride (PVDF, Arkema Inc.) and conductive agent s(Super C65, TIMCAL Ltd.) with a ratio of 8:1:1 to prepare the electrode. The mix was then well dissolved in a proper amount of *N*-methyl-2-pyrrolidone (NMP, ≥ 99%, Sigma-Aldrich) and mixed with a Thinky Mixer (Thinky Corporation) to form the slurry. The slurry was cast onto Al foil and dried at 80 °C in a vacuum oven for 12 h followed by 1 h of 120 °C drying at elevated temperature. The electrode was punched into cathode discs with a 12.7 mm diameter and a loading of active mass around 12 mg cm^{-2}. Several other LRLO samples were also studied in this work to show the reproducibility of the cycling performance improvement through LiBOB-containing electrolyte, including Li$_{1.144}$Ni$_{0.136}$Co$_{0.136}$Mn$_{0.544}$O$_2$ (denoted as LRLO-NIMTE), Li$_{1.12}$Ni$_{0.35}$Mn$_{0.53}$O$_2$ (denoted as LRLO-UMB), Li$_{1.19}$Ni$_{0.22}$Mn$_{0.58}$Co$_{0.01}$O$_2$ (denoted as LRLO-UMC), and Li$_{1.14}$Ni$_{0.35}$Mn$_{0.52}$O$_2$ (denoted as LRLO-UMD). Here LRLO-NIMTE is provided by Ningbo Institute of Materials Technology & Engineering (NIMTE); LRLO-UMB, LRLO-UMC, and LRLO-UMD are provided by Umicore. For LRLO/Li half cells, a Li metal chip with 1mm thickness was used as the anode and the cells were assembled as CR2016 coin cells. For LRLO/graphite full cells, both CR2032 and pouch cells were assembled. The graphite electrode used in this work is provided by NIMTE with an active mass ratio of 95%. For CR2032 full cells, the graphite electrode was punched into anode discs with 13 mm diameter and the designed N/P ratio was around 1.13. For pouch-type full cells, the cathode size was 44 × 30 mm and the anode size was 45 × 32 mm. For all the cells, Celgard 2325 was used as the separator. 1M LiPF$_6$ in EC:DMC = 3:7 (vol%) was obtained from Gotion, USA and is denoted as baseline electrolyte in the following sessions. 1M LiPF$_6$ in EC:DMC = 3:7 (vol%) + 2 wt% LiBOB was mixed from baseline electrolyte and the LiBOB salt (Sigma-Aldrich). This electrolyte is denoted as LiBOB electrolyte in the following sessions. All the coin cells were assembled

in the Ar-filled glovebox with moisture control (H$_2$O < 0.5 ppm) and 50 μl of electrolyte was used for each coin cell. The pouch cells were first assembled in the atmosphere without electrolyte. After that, the pouch cell was moved to a heating tray inside the glovebox antechamber and dried at 80 °C overnight under vacuum before the electrolyte injection. After drying, the dry pouches were moved inside the Ar-filled glovebox without air exposure and 500 μl of electrolyte was injected into each cell. The pouch cells with electrolyte were then vacuum sealed inside the glovebox and moved out for further testing. After assembling, the half cells were tested between 2.0 and 4.8 V at C/20 for the first cycle and C/10 for the rest of cycling (1 C = 250 mA g^{-1}). The coin cell and pouch cell full cells were tested between 2.0 and 4.7 V at C/20 for the first cycle (1 C = 270 mA g^{-1}) and 2.0–4.55 V at C/10 or C/3 for the rest of cycling. The detailed testing conditions for these cells can be found in Table S3-S5. The electrochemical performances of all the cells were tested at room temperature either by Neware Battery Test System (Neware Technology Ltd., China) or Arbin BT2000 instruments (Arbin instrument, USA).

Materials Characterizations: The LRLO-UM/graphite full cells were disassembled inside an Ar-filled glovebox after cycling. All the cell components were separated by plastic tweezer to avoid potential cell shortage. For electrolyte-soaked samples, a pristine electrode is soaked in electrolyte overnight for each sample. To preserve the surface species generated on the electrode during cycling or electrolyte soaking, all the electrode samples were not washed with any solvents after cell disassembling or electrolyte soaking. The unwashed electrodes were stored inside the glovebox before further characterization. Scanning electron microscope (SEM) with energy dispersive X-ray spectroscopy (EDX) was conducted with FEI Apreo to characterize the morphology and elemental distribution of the materials. The samples were briefly (<10 s) exposed to air when transferred inside the SEM. The SEM images were taken with Everhart-Thornley Detectors (ETD) detector with an accelerating voltage of 5.0 kV and a working distance of 10 mm. The EDX data were collected with an accelerating voltage of 20.0 kV and a working distance of 10 mm. For each sample, EDX results are collected with at least 3 spots. X-ray diffraction (XRD) patterns of the materials were collected at 11-BM in Advanced Photon Source (APS) at Argonne National Laboratory with a wavelength of 0.4579 Å. Rietveld refinement was applied to the obtained diffraction pattern using GSAS-II[100] software. X-ray photoelectron spectroscopy (XPS) was performed using a Kratos Axis Supra spectrometer with an Al anode source operated at 15 kV. All the XPS samples were prepared inside an Ar-filled glovebox and transferred to the XPS chamber under N$_2$ atmosphere. Transmission electron microscopy (TEM) was performed on a field emission gun JEOL2800 at 200 kV with Gatan OneView Camera (full 4k × 4k resolution). Scanning transmission electron microscopy (STEM) and electron energy loss spectroscopy (EELS) was performed on primary particles at the annular dark-field (ADF) mode using a JEOL JEM-ARM300CF at 300 kV, equipped with double correctors. To minimize possible electron beam irradiation effects, EELS spectra presented in this work were acquired from areas without pre-beam irradiation. Note that (S)TEM–EELS was carried out under cryogenic temperature (−180 °C) to minimize beam damage influence on CEI structure/chemistry. To prepare TEM samples, powder samples were dispersed on a lacey carbon grid inside the Ar glovebox. The loading and transferring grids to TEM were carefully executed to prevent air exposure. Cryo-focused ion beam (cryo-FIB) was used to prepare the lamella samples for STEM-EELS analysis through an FEI Scios DualBeam. A platinum protecting layer was deposited on the particles before the milling. A gallium ion beam source was used to mill and thin the sample. The lower operating voltages of the ion beam at 16 kV and 8 kV were used to thin and clean the lamella. The loading and transferring of the lamella to STEM were also carefully executed to prevent air exposure.

Electrolyte Characterizations: After cycling, the pouch cells were cut open in an Ar-filled glovebox and the cycled electrolyte was carefully squeezed out into a plastic microcentrifuge tube and stored inside the glovebox. Inductively coupled plasma mass spectrometry (ICP-MS) was performed with a Thermo iCAP RQ ICP-MS to analyze the elemental concentration in fresh and cycled electrolytes. Since the Li and B amounts in the electrolytes are much larger than Ni, Co and Mn, two different ICP

sample preparation recipes were used. For Ni, Co, and Mn concentration analysis, 50 µl of the electrolyte was diluted with ICP matrix solution (0.5% HCl + 0.5% HNO$_3$ in H$_2$O) to form 3 ml of ICP sample. For Li and B concentration analysis, 10 µl of the electrolyte was diluted with matrix solution to form 25 ml initial-mixed sample, and 500 µl of the initial-mixed sample was extracted and diluted with matrix solution to form 10 ml of ICP sample. An electrolyte density of 1.2 g ml^{-1} was used in ICP-MS calculations. Karl-Fischer Titration (KF Titration) was performed with an AQ-300 Coulometric Karl Fischer Titrator to determine the moisture level in the electrolyte. For each titration, 10 µl of electrolyte was collected with a micro-syringe inside the Ar-filled glovebox. The syringe was then taken out of the glovebox and the electrolyte was injected into the titrator immediately. Two to three titrations were performed on each sample. Nuclear magnetic resonance spectroscopy (NMR) was conducted on electrolytes to analyze the salt species in the electrolyte. The NMR measurements of the electrolyte samples were performed with a Jeol ECA 500 spectrometer. For each NMR sample, 120 µl of electrolyte was mixed with 360 µl anhydrous deuterated dimethyl sulfoxide (d-DMSO) to form a clear solution, and 50 µl of α, α, α-Trifluorotoluene was added to each sample as the reference. The NMR sample was then sealed in an NMR tube inside the Ar-filled glovebox for further measurement. The NMR spectrums were analyzed with MestReNova. All spectrums were calibrated with α, α, α-Trifluorotoluene at −63.72 ppm.

Supporting Information

Supporting Information is available from the Wiley Online Library or from the author.

Acknowledgements

Conflict of Interest

The authors declare no conflict of interest.

Authors Contribution

Y.L., M.Z., and Y.S.M. designed the experiments. Y.L. conducted electrochemistry testing, SEM-EDX, XRD, NMR testing, and data analysis. H.N.N., J.P., and S.K. designed and conducted the cathode material synthesis. W.L. conducted XPS measurement. R.S. conducted the ICP measurement. Y.L. conducted XPS and ICP data analysis. D.C.

conducted cryo-FIB and sample lamella preparation. M.Z. conducted cryo-TEM and cryo-STEM-EELS experiments and analysis. Y.S.M. and M.Z. supervised the research. Y.L wrote the manuscript. All authors contributed to the discussion and provided feedback on the manuscript.

Data Availability Statement

The data that support the findings of this study are available from the corresponding author upon reasonable request.

Keywords

[1] Y. Li, Y. Bai, X. Bi, J. Qian, L. Ma, J. Tian, C. Wu, F. Wu, J. Lu, K. Amine, *ChemSusChem* **2016**, *9*, 728.

[2] B. Lee, Z. Wu, V. Petrova, X. Xing, H. Lim, H. Liu, P. Liu, *J. Electrochem. Soc.* **2018**, *165*, A525.

[3] D. Mohanty, J. Li, D. P. Abraham, A. Huq, E. A. Payzant, D. L. Wood, C. Daniel, *Chem. Mater.* **2014**, *26*, 6272.

[4] B. Xu, C. R. Fell, M. Chi, Y. S. Meng, *Energy Environ. Sci.* **2011**, *4*, 2223.

[5] E. McCalla, A. M. Abakumov, M. Saubanere, D. Foix, E. J. Berg, G. Rousse, M.-L. Doublet, D. Gonbeau, P. Novak, G. Van Tendeloo, R. Dominko, J.-M. Tarascon, *Science* **2015**, *350*, 1516.

[6] R. A. House, U. Maitra, M. A. Pérez-Osorio, J. G. Lozano, L. Jin, J. W. Somerville, L. C. Duda, A. Nag, A. Walters, K. J. Zhou, M. R. Roberts, P. G. Bruce, *Nature* **2020**, *577*, 502.

[7] A. Singer, S. Hy, M. Zhang, D. Cela, C. Fang, B. Qiu, Y. Xia, Z. Liu, A. Ulvestad, N. Hua, J. Wingert, H. Liu, M. Sprung, A. V. Zozulya, E. Maxey, R. Harder, Y. S. Meng, O. G. Shpyrko, *Nat. Energy* **2017**, *3*, 641.

[8] C. R. Fell, D. Qian, K. J. Carroll, M. Chi, J. L. Jones, Y. S. Meng, *Chem. Mater.* **2013**, *25*, 1621.

[9] A. R. Armstrong, M. Holzapfel, P. Novák, C. S. Johnson, S. H. Kang, M. M. Thackeray, P. G. Bruce, *J. Am. Chem. Soc.* **2006**, *128*, 8694.

[10] D. Qian, B. Xu, M. Chi, Y. S. Meng, *Phys. chem. chem. phys.* **2014**, *16*, 14665.

[11] A. Ito, Y. Sato, T. Sanada, M. Hatano, H. Horie, Y. Ohsawa, *J. Power Sources* **2011**, *196*, 6828.

[12] C. R. Fell, M. Chi, Y. S. Meng, J. L. Jones, *Solid State Ionics* **2012**, *207*, 44.

[13] G. Kobayashi, Y. Irii, F. Matsumoto, A. Ito, Y. Ohsawa, S. Yamamoto, Y. Cui, J.-Y. Son, Y. Sato, *J. Power Sources* **2016**, *303*, 250.

[14] J. M. Zheng, Z. R. Zhang, X. B. Wu, Z. X. Dong, Z. Zhu, Y. Yang, *J. Electrochem. Soc.* **2008**, *155*, A775.

[15] X. Zhang, I. Belharouak, L. Li, Y. Lei, J. W. Elam, A. Nie, X. Chen, R. S. Yassar, R. L. Axelbaum, *Adv. Energy Mater.* **2013**, *3*, 1299.

[16] M. Lengyel, K. Y. Shen, D. M. Lanigan, J. M. Martin, X. Zhang, R. L. Axelbaum, *J. Mater. Chem. A* **2016**, *4*, 3538.

[17] T. A. Wynn, C. Fang, M. Zhang, H. Liu, D. M. Davies, X. Wang, D. Lau, J. Z. Lee, B. Y. Huang, K. Z. Fung, C. T. Ni, Y. S. Meng, *J. Mater. Chem. A* **2018**, *6*, 24651.

**ADVANCED
SCIENCE NEWS**
www.advancedsciencenews.com

**ADVANCED
ENERGY
MATERIALS**
www.advenergymat.de

[18] L. Li, B. H. Song, Y. L. Chang, H. Xia, J. R. Yang, K. S. Lee, L. Lu, *J. Power Sources* **2015**, *283*, 162.

[19] B. Qiu, M. Zhang, S.-Y. Lee, H. Liu, T. A. Wynn, L. Wu, Y. Zhu, W. Wen, C. M. Brown, D. Zhou, Z. Liu, Y. S. Meng, *Cell Rep. Phys. Sci.* **2020**, *1*, 100028.

[20] Y. Li, M. J. Zuba, S. Bai, Z. W. Lebens-Higgins, B. Qiu, S. Park, Z. Liu, M. Zhang, L. F. J. Piper, Y. S. Meng, *Energy Storage Mater.* **2021**, *35*, 99.

[21] W. Li, Y. G. Cho, W. Yao, Y. Li, A. Cronk, R. Shimizu, M. A. Schroeder, Y. Fu, F. Zou, V. Battaglia, A. Manthiram, M. Zhang, Y. S. Meng, *J. Power Sources* **2020**, *473*, 228579.

[22] M. Metzger, P. Walke, S. Solchenbach, G. Salitra, D. Aurbach, H. A. Gasteiger, *J. Electrochem. Soc.* **2020**, *167*, 160522.

[23] J. Han, K. Kim, Y. Lee, N. Choi, *Adv. Mater.* **2019**, *31*, 1804822.

[24] A. Guéguen, D. Streich, M. He, M. Mendez, F. F. Chesneau, P. Novák, E. J. Berg, *J. Electrochem. Soc.* **2016**, *163*, A1095.

[25] M. Liu, J. Vatamanu, X. Chen, L. Xing, K. Xu, W. Li, *ACS Energy Lett.* **2021**, *6*, 2096.

[26] C. Zhan, T. Wu, J. Lu, K. Amine, *Energy Environ. Sci.* **2018**, *11*, 243.

[27] J. Asenbauer, T. Eisenmann, M. Kuenzel, A. Kazzazi, Z. Chen, D. Bresser, *Sustainable Energy Fuels* **2020**, *4*, 5387.

[28] L. Wang, Y. Ma, Q. Li, Z. Zhou, X. Cheng, P. Zuo, C. Du, Y. Gao, G. Yin, *J. Power Sources* **2017**, *361*, 227.

[29] X. Zheng, X. Wang, X. Cai, L. Xing, M. Xu, Y. Liao, X. Li, W. Li, *ACS Appl. Mater. Interfaces* **2016**, *8*, 30116.

[30] J. Lan, Q. Zheng, H. Zhou, J. Li, L. Xing, K. Xu, W. Fan, L. Yu, W. Li, *ACS Appl. Mater. Interfaces* **2019**, *11*, 28841.

[31] F. Lian, Y. Li, Y. He, H. Guan, K. Yan, W. Qiu, K. C. Chou, P. Axmann, M. Wohlfahrt-Mehrens, *RSC Adv.* **2015**, *5*, 86763.

[32] J. Cha, J. G. Han, J. Hwang, J. Cho, N. S. Choi, *J. Power Sources* **2017**, *357*, 97.

[33] J. Zhao, Y. Liang, X. Zhang, Z. Zhang, E. Wang, S. He, B. Wang, Z. Han, J. Lu, K. Amine, H. Yu, *Adv. Funct. Mater.* **2021**, *31*, 2009192.

[34] W. Liu, J. Li, W. Li, H. Xu, C. Zhang, X. Qiu, *Nat. Commun.* **2020**, *11*, 3629.

[35] S. Brutti, E. Simonetti, M. De Francesco, A. Sarra, A. Paolone, O. Palumbo, S. Fantini, R. Lin, A. Falgayrat, H. Choi, M. Kuenzel, S. Passerini, G. B. Appetecchi, *J. Power Sources* **2020**, *479*, 228791.

[36] J. Im, J. Lee, M.-H. Ryou, Y. M. Lee, K. Y. Cho, *J. Electrochem. Soc.* **2017**, *164*, A6381.

[37] H. Q. Pham, E. H. Hwang, Y. G. Kwon, S. W. Song, *Adv. Mater. Interfaces* **2017**, *4*, 1700483.

[38] J. H. Song, A. Kapylou, H. S. Choi, B. Y. Yu, E. Matulevich, S. H. Kang, *J. Power Sources* **2016**, *313*, 65.

[39] Y. Zhu, J. Yang, G. Cheng, K. Carroll, O. Clemons, D. Strand, *Novel Non-Carbonate Based Electrolytes for Silicon Anodes*, Pittsburgh, PA, and Morgantown, WV (United States), **2016**.

[40] T. Noguchi, T. Hasegawa, H. Yamauchi, I. Yamazaki, K. Utsugi, *ECS Trans.* **2017**, *80*, 291.

[41] C. C. Su, M. He, P. C. Redfern, L. A. Curtiss, I. A. Shkrob, Z. Zhang, *Energy Environ. Sci.* **2017**, *10*, 900.

[42] N. Ehteshami, E. Paillard, *ECS Trans.* **2017**, *77*, 11.

[43] N. Ehteshami, A. Eguia-Barrio, I. de Meatza, W. Porcher, E. Paillard, *J. Power Sources* **2018**, *397*, 52.

[44] W. Xu, C. A. Angell, *Electrochem. Solid-State Lett.* **2001**, *4*, E1.

[45] U. Lishka, U. Wietelmann, M. Wegner, *Part.DE 19829030 C1*, **1999**.

[46] K. Xu, S. Zhang, T. R. Jow, W. Xu, C. A. Angell, *Electrochem. Solid-State Lett.* **2002**, *5*, A26.

[47] S. T. Myung, H. Natsui, Y. K. Sun, H. Yashiro, *J. Power Sources* **2010**, *195*, 8297.

[48] K. Xu, S. S. Zhang, U. Lee, J. L. Allen, T. R. Jow, *J. Power Sources* **2005**, *146*, 79.

[49] M. Xu, L. Zhou, Y. Dong, Y. Chen, A. Garsuch, B. L. Lucht, *J. Electrochem. Soc.* **2013**, *160*, A2005.

[50] S. Dalavi, M. Xu, B. Knight, B. L. Lucht, *Electrochem. Solid-State Lett.* **2011**, *15*, A28.

[51] V. Aravindan, Y. L. Cheah, W. C. Ling, S. Madhavi, *J. Electrochem. Soc.* **2012**, *159*, A1435.

[52] Z. Xiao, J. Liu, G. Fan, M. Yu, J. Liu, X. Gou, M. Yuan, F. Cheng, *Mater. Chem. Front.* **2020**, *4*, 1689.

[53] X. Bian, S. Ge, Q. Pang, K. Zhu, Y. Wei, B. Zou, F. Du, D. Zhang, G. Chen, *J. Alloys Compd.* **2018**.

[54] M. Xu, N. Tsiouvaras, A. Garsuch, H. A. Gasteiger, B. L. Lucht, *J. Phys. Chem. C* **2014**, *118*, 37.

[55] Y. Dong, B. T. Young, Y. Zhang, T. Yoon, D. R. Heskett, Y. Hu, B. L. Lucht, *ACS Appl. Mater. Interfaces* **2017**, *9*, 20467.

[56] P. K. Nayak, J. Grinblat, M. Levi, D. Aurbach, *J. Electrochem. Soc.* **2015**, *162*, A596.

[57] J. Zhang, Q. Zhang, D. Wong, N. Zhang, G. Ren, L. Gu, C. Schulz, L. He, Y. Yu, X. Liu, *Nat. Commun.* **2021**, *12*, 3071.

[58] Z. Wei, W. Zhang, F. Wang, Q. Zhang, B. Qiu, S. Han, Y. Xia, Y. Zhu, Z. Liu, *Chem.–Eur. J.* **2015**, *21*, 7503.

[59] J. L. Shi, J. N. Zhang, M. He, X. D. Zhang, Y. X. Yin, H. Li, Y. G. Guo, L. Gu, L. J. Wan, *ACS Appl. Mater. Interfaces* **2016**, *8*, 20138.

[60] J. Wang, X. He, E. Paillard, N. Laszczynski, J. Li, S. Passerini, *Adv. Energy Mater.* **2016**, *6*, 1600906.

[61] Z. Lu, L. Y. Beaulieu, R. A. Donaberger, C. L. Thomas, J. R. Dahn, *J. Electrochem. Soc.* **2002**, *149*, A778.

[62] Z. Lu, J. R. Dahn, *J. Electrochem. Soc.* **2002**, *149*, A815.

[63] D.-H. Seo, J. Lee, A. Urban, R. Malik, S. Kang, G. Ceder, *Nat. Chem.* **2016**, *8*, 692.

[64] G. Assat, J. M. Tarascon, *Nat. Energy* **2018**, *3*, 373.

[65] W. Li, Y.-G. Cho, W. Yao, Y. Li, A. Cronk, R. Shimizu, M. A. Schroeder, Y. Fu, F. Zou, V. Battaglia, A. Manthiram, M. Zhang, Y. S. Meng, *J. Power Sources* **2020**, *473*, 228579.

[66] M. M. Thackeray, S.-H. Kang, C. S. Johnson, J. T. Vaughey, R. Benedek, S. A. Hackney, *J. Mater. Chem.* **2007**, *17*, 3112.

[67] M. Ko, P. Oh, S. Chae, W. Cho, J. Cho, *Small* **2015**, *11*, 33.

[68] B. Qiu, M. Zhang, Y. Xia, Z. Liu, Y. S. Meng, *Chem. Mater.* **2017**, *29*, 908.

[69] G. Assat, D. Foix, C. Delacourt, A. Iadecola, R. Dedryvère, J.-M. Tarascon, *Nat. Commun.* **2017**, *8*, 2219.

[70] J.-L. Shi, J.-N. Zhang, M. He, X.-D. Zhang, Y.-X. Yin, H. Li, Y.-G. Guo, L. Gu, L.-J. Wan, *ACS Appl. Mater. Interf aces* **2016**, *8*, 20138.

[71] S. Jiao, X. Ren, R. Cao, M. H. Engelhard, Y. Liu, D. Hu, D. Mei, J. Zheng, W. Zhao, Q. Li, N. Liu, B. D. Adams, C. Ma, J. Liu, J.-G. Zhang, W. Xu, *Nat. Energy* **2018**, *3*, 739.

[72] M. Xu, N. Tsiouvaras, A. Garsuch, H. A. Gasteiger, B. L. Lucht, *J. Phys. Chem. C* **2014**, *118*, 7363.

[73] S. Y. Ha, J. G. Han, Y. M. Song, M. J. Chun, S. Il Han, W. C. Shin, N. S. Choi, *Electrochim. Acta* **2013**, *104*, 170.

[74] C. Cui, X. Fan, X. Zhou, J. Chen, Q. Wang, L. Ma, C. Yang, E. Hu, X.-Q. Yang, C. Wang, *J. Am. Chem. Soc.* **2020**, *142*, 8918.

[75] E. Zhao, M. Zhang, X. Wang, E. Hu, J. Liu, X. Yu, M. Olguin, T. A. Wynn, Y. S. Meng, K. Page, F. Wang, H. Li, X.-Q. Yang, X. Huang, L. Chen, *Energy Storage Mater.* **2020**, *24*, 384.

[76] S. Park, S. Y. Jeong, T. K. Lee, M. W. Park, H. Y. Lim, J. Sung, J. Cho, S. K. Kwak, S. Y. Hong, N.-S. Choi, *Nat. Commun.* **2021**, *12*, 838.

[77] C. Tan, J. Yang, Q. Pan, Y. Li, Y. Li, L. Cui, X. Fan, F. Zheng, H. Wang, Q. Li, *Chem. Eng. J.* **2021**, *410*, 128422.

[78] M. Diehl, M. Evertz, M. Winter, S. Nowak, *RSC Adv.* **2019**, *9*, 12055.

[79] M. Y. Abeywardana, N. Laszczynski, M. Kuenzel, D. Bresser, S. Passerini, B. Lucht, *Int. J. Electrochem.* **2019**, *2019*, 1.

[80] B. S. Parimalam, A. D. MacIntosh, R. Kadam, B. L. Lucht, *J. Phys. Chem. C* **2017**, *121*, 22733.

[81] M. Nie, B. L. Lucht, *J. Electrochem. Soc.* **2014**, *161*, A1001.

**ADVANCED
SCIENCE NEWS**

www.advancedsciencenews.com

**ADVANCED
ENERGY
MATERIALS**

www.advenergymat.de

[82] R. Weber, M. Genovese, A. J. Louli, S. Hames, C. Martin, I. G. Hill, J. R. Dahn, *Nat. Energy* **2019**, *4*, 683.

[83] D. Lu, G. Xu, Z. Hu, Z. Cui, X. Wang, J. Li, L. Huang, X. Du, Y. Wang, J. Ma, X. Lu, H. J. Lin, C. Te Chen, A. A. Nugroho, L. H. Tjeng, G. Cui, *Small Methods* **2019**, *3*, 1900546.

[84] A. Xiao, L. Yang, B. L. Lucht, *Electrochem. Solid-State Lett.* **2007**, *10*, A241.

[85] N.-S. Choi, J.-G. Han, S.-Y. Ha, I. Park, C.-K. Back, *RSC Adv.* **2015**, *5*, 2732.

[86] A. J. Louli, A. Eldesoky, R. Weber, M. Genovese, M. Coon, J. deGooyer, Z. Deng, R. T. White, J. Lee, T. Rodgers, R. Petibon, S. Hy, S. J. H. Cheng, J. R. Dahn, *Nat. Energy* **2020**, *5*, 693.

[87] N. Schulz, R. Hausbrand, C. Wittich, L. Dimesso, W. Jaegermann, *J. Electrochem. Soc.* **2018**, *165*, A833.

[88] B. Philippe, M. Hahlin, K. Edström, T. Gustafsson, H. Siegbahn, H. Rensmo, *J. Electrochem. Soc.* **2016**, *163*, A178.

[89] S. J. An, J. Li, C. Daniel, D. Mohanty, S. Nagpure, D. L. Wood, *Carbon* **2016**, *105*, 52.

[90] V. Aravindan, J. Gnanaraj, S. Madhavi, H.-K. Liu, *Chem.–Eur. J.* **2011**, *17*, 14326.

[91] S. S. Zhang, K. Xu, T. R. Jow, *J. Power Sources* **2006**, *156*, 629.

[92] K. Xu, S. Zhang, T. R. Jow, *Electrochem. Solid-State Lett.* **2005**, *8*, A365.

[93] J. Zhang, J. Yang, L. Yang, H. Lu, H. Liu, B. Zheng, *Mater. Adv.* **2021**, *2*, 1747.

[94] M. Metzger, J. Sicklinger, D. Haering, C. Kavakli, C. Stinner, C. Marino, H. A. Gasteiger, *J. Electrochem. Soc.* **2015**, *162*, A1227.

[95] M. Metzger, B. Strehle, S. Solchenbach, H. A. Gasteiger, *J. Electrochem. Soc.* **2016**, *163*, A1219.

[96] L. Xing, W. Li, C. Wang, F. Gu, M. Xu, C. Tan, J. Yi, *J. Phys. Chem. B* **2009**, *113*, 16596.

[97] J. D. Cox, D. D. Wagman, V. A. Medvedev, *CODATA Key Values for Thermodynamics*, Hemisphere Publishing Corp., New York **1989**.

[98] T. L. Cottrell, *The Strengths of Chemical Bonds*, Butterworths Scientific Publications, London **1958**.

[99] L. D. Ellis, I. G. Hill, K. L. Gering, J. R. Dahn, *J. Electrochem. Soc.* **2017**, *164*, A2426.

[100] B. H. Toby, R. B. Von Dreele, *J. Appl. Crystallogr.* **2013**, *46.2*, 544.